J. Fluid Mech. (2015), *vol.* 779, *pp.* 116–143.
doi:10.1017/jfm.2015.366

Confined turbulent entrainment across density interfaces

Ajay B. Shrinivas[1] **and Gary R. Hunt**[2,†]

[1]Department of Civil and Environmental Engineering, Imperial College London, London SW7 2AZ, UK

[2]Department of Engineering, University of Cambridge, Trumpington Street, Cambridge CB2 1PZ, UK

(Received 14 October 2014; revised 10 May 2015; accepted 24 June 2015;
first published online 14 August 2015)

In pursuit of a universal law for the rate of entrainment across a density interface driven by the impingement of a localised turbulent flow, the role of the confinement, wherein the environment is within the confines of a box, has to date been overlooked. Seeking to unravel the effects of confinement, we develop a phenomenological model describing the quasi-steady rate at which buoyant fluid is turbulently entrained across a density interface separating two uniform layers within the confines of a box. The upper layer is maintained by a turbulent plume, and the localised impingement of a turbulent fountain with the interface drives entrainment of fluid from the upper layer into the lower layer. The plume and fountain rise from sources at the base of the box and are non-interacting. Guided by previous observations, our model characterises the dynamics of fountain–interface interaction and the steady secondary flow in the environment that is induced by the perpetual cycle of vertical excursions of the interface. We reveal that the dimensionless entrainment flux across the interface E_i is governed not only by an interfacial Froude number Fr_i but also by a 'confinement' parameter λ_i, which characterises the length scale of interfacial turbulence relative to the depth of the upper layer. By deducing the range of λ_i that may be regarded as 'small' and 'large', we shed new light on the effects of confinement on interfacial entrainment. We establish that for small λ_i, a weak secondary flow has little influence on E_i, which follows a quadratic power law $E_i \propto Fr_i^2$. For large λ_i, a strong secondary flow significantly influences E_i, which then follows a cubic power law $E_i \propto Fr_i^3$. Drawing on these results, and showing that for previous experimental studies λ_i exhibits wide variation, we highlight underlying physical reasons for the significant scatter in the existing measurements of the rate of interfacial entrainment. Finally, we explore the implications of our results for guiding appropriate choices of box geometry for experimentally and numerically examining interfacial entrainment.

Key words: convection, plumes/thermals, stratified flows

1. Introduction

We theoretically examine 'confined' interfacial entrainment, that is, the turbulent downward transport of buoyant fluid across a gravitationally stable horizontal density interface separating two uniform fluid masses within the confines of a box. The last five decades have witnessed an extensive series of experimental investigations in

† Email address for correspondence: gary.hunt@eng.cam.ac.uk

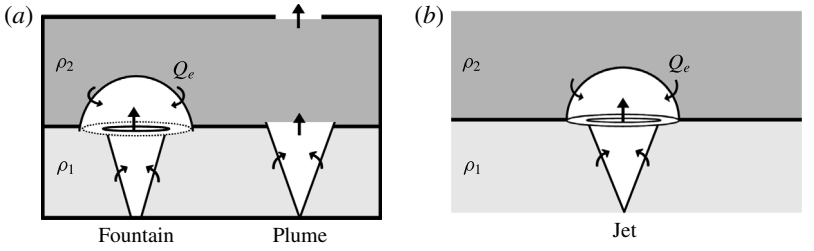

FIGURE 1. Schematics showing turbulent entrainment across an interface separating two uniform layers of densities ρ_1 (lower) and $\rho_2 < \rho_1$ (upper). A volume flux Q_e is entrained from the upper layer into the lower layer. (*a*) Layers confined in a box, as considered in this paper. A positively buoyant plume maintains the upper layer, a negatively buoyant impinging fountain drives interfacial entrainment, and a steady flow through a top opening into an external ambient is established. (*b*) The unconfined case, shown here with a neutrally buoyant impinging jet driving interfacial entrainment (cf. Shrinivas & Hunt 2014).

which turbulent entrainment across density interfaces is examined, by necessity, within the confines of a transparent box or visual tank. The rate of interfacial entrainment has historically been parameterised solely in terms of quantities local to the interface. However, in the pursuit of a universal entrainment law (for example relating the entrainment flux to an interfacial Froude number), the effects of confinement, i.e. the role of the box, on the dynamics of interfacial entrainment have not, to our knowledge, been examined explicitly until now. By unravelling the role of confinement, we herein challenge the notion of a universal entrainment law. Indeed, we deduce that the role of the box may be sufficient to explain a spread in measured entrainment rates from quadratic to cubic power laws.

From both experimental and theoretical viewpoints, it is appealing to investigate the classic transport phenomenon of interfacial entrainment (Fernando 1991) in a state of (quasi-) steady equilibrium. To this end, we consider the steady two-layer stratification established by a turbulent plume and a turbulent fountain in a box that connects to an external unbounded quiescent environment via an opening at the top. Figure 1(*a*) depicts the configuration we consider. The localised sources which give rise to the plume and the fountain are located at the base of the box and are sufficiently well separated so that the resulting plume and fountain are considered to be non-interacting. In the context of our study, the plume is essentially an artefact for enabling a buoyant upper layer of constant depth to be maintained. The impingement of the fountain with the interface, which separates the resulting upper layer from the fluid below (the lower layer), creates and sustains a localised turbulent region of eddying motions that drive entrainment of fluid across the interface. In other words, the plume establishes the two-layer stratification and the fountain provides the source of turbulence at the interface. As the flow, pre-impingement, is negatively buoyant relative to the lower layer, we refer to it as an impinging fountain. The appeal of this quasi-steady configuration is due to the steadiness eliminating the inherent complex time-dependent coupling between the entrainment flux across the interface and the evolution of a stratified intermediate layer. The main question we address is how does the confinement imposed by the physical boundaries of the box influence the rate of interfacial entrainment?

Our motivation to consider the role of confinement has been fuelled by the significant scatter in measurements of the entrainment rate. Coffey & Hunt (2010) comment that the underlying physical reason for this scatter is unknown and, as nominally identical configurations (e.g. plume/fountain impingement) and techniques have been used to induce and measure the entrainment rate, the scatter cannot be explained by experimental variabilities or systematic errors alone. Moreover, conflicting entrainment laws that stem from existing data currently shroud the understanding of the problem, thereby casting doubt on the most appropriate empirical entrainment model for application in engineering flows, the atmospheric sciences or oceanography, where interfacial entrainment is ubiquitous. Many of these applications are discussed in the review on mixing in stratified fluids by Fernando (1991).

With the aim of quantifying the volume flux Q_e entrained across a density interface, Shrinivas & Hunt (2014) analysed the large-time quasi-steady flow in an unconfined environment that is induced, and maintained, by the impingement of a turbulent axisymmetric jet on an interface separating two layers of uniform densities ρ_1 and $\rho_2 < \rho_1$ (figure 1*b*). Drawing on the wealth of previous observations, Shrinivas & Hunt (2014) modelled impingements with a small interfacial Froude number (Fr_i) as a semi-ellipsoidal dome and characterised large-Fr_i impingements as a fully penetrating turbulent fountain. For the high-Reynolds-number and high-Péclet-number flows of interest, the dimensionless entrainment flux

$$E_i = \frac{Q_e}{\pi b_i^2 w_i} \tag{1.1}$$

is governed solely by the interfacial Froude number $Fr_i = w_i/\sqrt{b_i \Delta g'}$, a quantity which characterises the relative strengths of the inertial forcing associated with the energy-containing eddies that drive interfacial entrainment and the buoyancy force that acts to stabilise the interface. Here, b_i and w_i denote the characteristic length scale and velocity scale at the interface (the radius and vertical velocity of the jet at the interface, respectively) and $\Delta g' = g(\rho_1 - \rho_2)/\rho_1$ the buoyancy step in the environment across the interface. Shrinivas & Hunt (2014) showed that $E_i \propto Fr_i^2$ for small Fr_i and $E_i \propto Fr_i$ for large Fr_i. Figure 2 plots the solution for this unconfined entrainment model together with the experimental data from Baines (1975), Kumagai (1984), Baines, Corriveau & Reedman (1993) and Lin & Linden (2005). These experimental studies measured interfacial entrainment driven by the localised impingement of a turbulent axisymmetric plume (Baines 1975; Kumagai 1984) or a turbulent axisymmetric fountain (Baines *et al.* 1993; Lin & Linden 2005). A comprehensive review of these and other previous studies is given in Shrinivas & Hunt (2014). Whilst the general trends are well captured by Shrinivas & Hunt's (2014) model (figure 2), it is evident that there is a significant spread in both the individual and collective data sets, with experimental values of E_i differing by an order of magnitude for a given Fr_i. These disparities compound the inherent challenges and uncertainties experimentalists face when pursuing an entrainment law of the form $E_i \propto Fr_i^n$. Owing to the complexities associated with an experimental approach, there is wide variation in the reported values of the exponent n, which include $n = 0$ (Lin & Linden 2005), $n = 1$ (Baines *et al.* 1993), $n = 2$ (Cardoso & Woods 1993; Ching, Fernando & Noh 1993) and $n = 3$ (Baines 1975; Coffey & Hunt 2010). Although the model developed by Shrinivas & Hunt (2014) elucidates the dominant physics at the heart of the quadratic and linear power laws, it does not explain the cubic power law.

Box confinement is an intrinsic feature of all the aforementioned experiments and the disparities between the reported entrainment laws are irrefutable. This raises

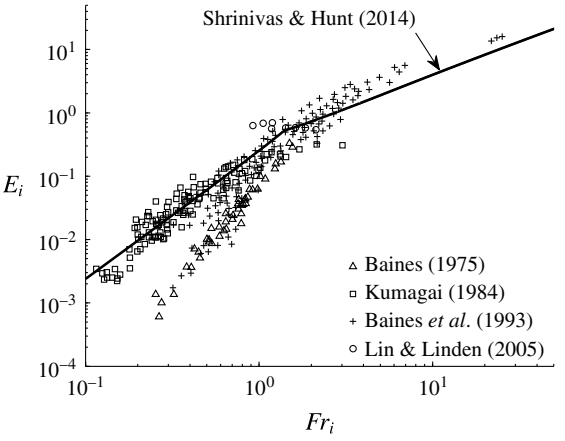

FIGURE 2. Dimensionless entrainment flux E_i against the interfacial Froude number Fr_i: comparison of the theoretical prediction of Shrinivas & Hunt (2014) (solid line) with previous experimental measurements. The theoretical prediction approximates to $E_i = 0.24Fr_i^2$ for $Fr_i < 1.4$ and $E_i = 0.42Fr_i$ for $Fr_i > 3.8$.

the question of whether interfacial entrainment and confinement are inextricably intertwined – confinement leading to secondary flows in the environment and secondary flows influencing measurements of the entrainment flux. Jirka & Harleman (1979) demonstrated that turbulent jets and plumes in a confined uniform fluid of finite depth induce a clearly defined flow pattern: a momentum jet forming circulation cells, and a buoyant plume forming a gravity current and a horizontal return flow. Ching *et al.* (1993) studied the interaction of a turbulent line plume with the density interface of a two-layer fluid within the confines of a box whose width W far exceeded its height H (figure 3*a*). Subsequent to its impingement with the interface, the plume formed an interfacial gravity current. Akin to the experiments of Jirka & Harleman (1979), they identified that horizontal secondary flows prevailed in the confined environment. Jirka & Harleman (1979) reported that entrainment into a jet/plume is influenced by secondary flows, and thus it is entirely conceivable that secondary flows in a confined two-layer system influence or modify interfacial entrainment.

Figure 3(*b*) shows a vertical profile of the horizontal velocity u in the environment measured by Ching *et al.* (1993). A flow in the upper layer, towards the interfacial dome, occurs by virtue of two independent mechanisms, which we now discuss in turn. First, plume impingement gives rise to a perpetual cycle of vertical excursions of the density interface (Ching *et al.* 1993), and the surplus potential energy that becomes available, as a result of the interfacial deflections, is converted into kinetic energy that drives a bulk flow in the environment. This available potential energy is stored in the horizontal density gradients that manifest when the interface deflects. Entrainment into the dome (figure 3*a*) and the requirement for volume conservation is the second mechanism by which a flow is induced in the upper layer. If we ignore the flow produced by interfacial deflections and consider just the mean velocity u_{in} of the flow induced by entrainment, continuity across a vertical section of the upper layer of depth D requires $Q_e = u_{in}WD$, that is, $u_{in}/w_i = E_i a_i/(WD)$. The area a_i of the localised impingement region is typically a small fraction of the box cross-sectional area (we note that $a_i < 0.1WD$ for the experiments of Ching *et al.* (1993)) and $E_i \ll 1$

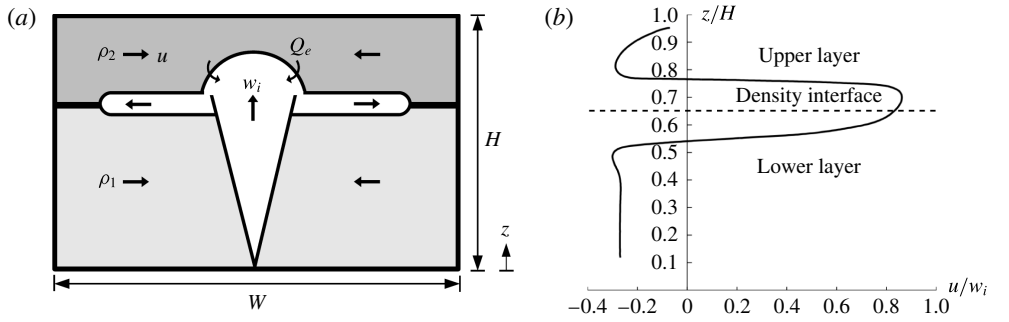

FIGURE 3. (*a*) Schematic showing the set-up considered by Ching *et al.* (1993), in which a turbulent line plume impinges on a density interface within the confines of a box. (*b*) Vertical profile of the dimensionless horizontal velocity u/w_i in the environment measured by Ching *et al.* (1993).

for small-Fr_i entrainment (figure 2). Thus, the flow induced by interfacial entrainment is weak, i.e. $u_{in}/w_i \ll 1$. However, figure 3 indicates that the velocity in the upper layer can be up to 30 % of w_i. We therefore expect that these relatively large velocities are primarily attributed to the flow produced by interfacial deflections. Hereinafter, we refer to the flow induced solely by the interfacial deflections as the 'secondary flow'.

Herein, by considering the steady two-layer stratification established by a plume and a fountain in a box, we determine the influence of confinement on interfacial entrainment and establish what the term 'confinement' signifies dynamically. In § 2, we develop a model of turbulent interfacial entrainment in the presence of a secondary flow induced by vertical excursions of the interface. We reveal that, besides Fr_i, E_i is dependent on a second dimensionless quantity, namely a 'confinement' parameter λ_i, which characterises the length scale of interfacial turbulence relative to the vertical extent of the confinement, so that in general $E_i = E_i(Fr_i, \lambda_i)$. Analysing the model predictions in § 3, we establish that for small λ_i, the secondary flow is weak and has little influence on E_i. Hence we regard interfacial entrainment in this regime as weakly confined. By contrast, E_i is significantly influenced by a strong secondary flow when λ_i is sufficiently large, and hence we regard interfacial entrainment in this regime as strongly confined. In these limits of small λ_i and large λ_i, the scaling of E_i on Fr_i is distinct, giving

$$E_i \propto \begin{cases} Fr_i^2 & \text{for } \lambda_i \ll \lambda_{i,c}, \\ Fr_i^3 & \text{for } \lambda_i \gg \lambda_{i,c}, \end{cases} \quad \lambda_{i,c} = 0.16 Fr_i^{-2}. \tag{1.2}$$

Our theory thereby offers a reason as to why some data sets support a cubic power law whilst others follow a quadratic power law. Deducing where possible the values of λ_i for previous experiments, we highlight physical reasons for the scatter in the existing data (figure 2). Drawing on our predictions, in § 4 we offer guidance on an appropriate box geometry and configuration for experimentally and numerically examining interfacial entrainment.

2. A model for confined interfacial entrainment

Based on the experimental observations of Jirka & Harleman (1979) and Ching *et al.* (1993), we hypothesise that secondary flows induced by the deflections of the interface within the confines of a box may influence or modify the dynamics of

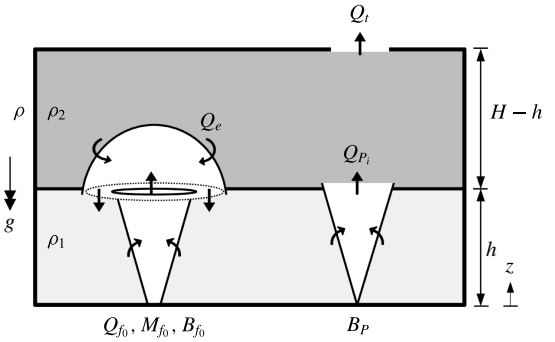

FIGURE 4. Schematic showing the steady two-layer flow established by a turbulent fountain (left) and a turbulent pure plume (right) with sources at the base ($z = 0$) of a box of height H. The steady density interface is at height $z = h$.

turbulent entrainment across a density interface. To investigate this hypothesis, we relax the condition of an unconfined environment and extend the model of Shrinivas & Hunt (2014) to describe interfacial entrainment within a box of height H and plan area S. The box interior connects to an unbounded quiescent ambient of uniform density ρ via an opening of area a_t at the top (figure 4). At the base of the box ($z = 0$), a continuous point source of constant buoyancy flux B_P gives rise to a turbulent axisymmetric pure plume, and the continuous vertically forced upward injection of relatively dense fluid from a circular area source (radius b_{f_0}), with constant fluxes of volume Q_{f_0}, momentum M_{f_0} and buoyancy $B_{f_0} < 0$, produces a turbulent axisymmetric fountain. The two sources are sufficiently well separated that the resulting plume and fountain are regarded as non-interacting. As confirmed in the experiments of Lin & Linden (2005), these sources establish two buoyant layers, separated by a steady interface at height $z = h$, as depicted in figure 4. The boundaries of the box are purely a physical constraint and there are no buoyancy exchanges between them and the fluid. Our system is a direct analogue of the experiments of Lin & Linden (2005) and of numerous others (§ 1) that have examined entrainment across interfaces by using saline releases in water to create density contrasts.

The minimum separation distance between the sources corresponds to the distance at which the plume and fountain first interact at the top of the box ($z = H$). Kaye & Linden (2004) showed that two plumes of similar strength coalesce at a height of approximately four times the separation of their sources. Thus, for a first approximation we may take the minimum separation distance between the sources as $H/4$. This is consistent with Lin & Linden's (2005) experiments.

At steady state, the fluxes of volume and buoyancy supplied via the sources are exactly matched by the corresponding fluxes driven, by the buoyant layers, out through the top opening. We assume that the flow through the opening remains unidirectional. Hunt & Coffey (2010) showed that a Froude number Fr_t associated with the flow through the top opening characterises the direction of flow and to achieve a unidirectional outflow requires $Fr_t > 0.33$. This requirement restricts the range of possible dimensionless opening areas a_t/H^2, as discussed in Hunt & Coffey (2010).

Our model is underpinned by the three key facets of interfacial entrainment noted by Turner (1986), namely, the dynamics of the energy source driving the entrainment, the entrainment mechanism and the influence of the energy source on the environment.

We now consider each of these in turn. First, energy for interfacial entrainment is channelled to the interface via the fountain, the dynamics of which are well described by existing models (see, for example, the review by Hunt & Burridge 2015). Second, the entrainment mechanism is attributed to the engulfment of fluid by baroclinic vortices around the periphery of the impingement dome. Shrinivas & Hunt (2014) developed a mechanistic description of this process and showed that, much as for plume entrainment, the entrainment velocity is proportional to a local vertical velocity. The third facet of the problem, namely that which pertains to the fountain–interface interaction and its influence on the two-layer stratification, has received little attention. We will see (§§ 2.2, 3) that fountain–interface interaction plays an instrumental role in the dynamics of confined interfacial entrainment.

Our system is similar to the experimental arrangement of Lin & Linden (2005). For a laboratory experiment our system would be inverted, with saline solution injected downwards, from a localised source, into a box of fresh water to generate a dense plume and by supplying fresh water downwards at the fountain source to produce a fountain in the steady state. For the Boussinesq flows of concern here, this reversal of direction of the buoyancy force is unimportant to the dynamics, apart from reversing the sense of motion. Following Lin & Linden (2005), we assume that the layers are of uniform density. Accordingly, the mean buoyancies

$$g_1' = g\left(\frac{\rho-\rho_1}{\rho}\right) \quad \text{and} \quad g_2' = g\left(\frac{\rho-\rho_2}{\rho}\right) \tag{2.1a,b}$$

are assigned to the lower layer of density ρ_1 and the upper layer of density ρ_2, respectively. The measurements of Lin & Linden (2005) showed that this is a very good assumption for the upper layer. Turbulent fluctuations associated with the downward entrainment flux across the interface give rise to weak density gradients adjacent to the interface. However, these gradients are confined in a relatively thin transitional region ($\sim 0.1H$), and so to a first approximation we assume two uniform layers.

Entrainment of fluid from the upper layer into the lower layer is driven by energetic eddying motions contained within a localised region of turbulent flow above the interface (shown as a dome in figure 4) resulting from the impingement of the fountain. The morphology and dynamics of this turbulent flow above the interface are governed primarily by the interfacial Froude number

$$Fr_i = \frac{w_i}{\sqrt{b_i \Delta g'}}, \quad \Delta g' = g_2' - g_1', \tag{2.2a,b}$$

where w_i and b_i are the mean vertical velocity and mean radius of the fountain at the interface. When Fr_i is small ($Fr_i \lesssim 1$), the interfacial impingement is weakly energetic (Shrinivas & Hunt 2014), and strong buoyancy forces local to the interface arrest the penetration of dense fluid, resulting in the formation of a shallow dome-like upwelling (figure 4). This behaviour and morphology of flow is confirmed by several experimental studies (Kumagai 1984; Shy 1995; Hunt & Coffey 2010). The shadowgraph images from Hunt & Coffey's (2010) experiments clearly indicate the presence of impingement domes (figure 5). A volume flux Q_e of buoyant fluid is entrained from the upper layer into the dome by baroclinic vortices around the periphery of the dome. The entrained fluid is transported downwards across the interface through an annular region. Our attention is centred around these small-Fr_i flows, and we shall restrict our model to $Fr_i < 1.4$ (Shrinivas & Hunt 2014). In § 2.1, we relate Q_e to the interface position ($z = h$) and the layer buoyancies (g_1', g_2') by considering conservation arguments for the buoyant layers. In §§ 2.2 and 2.3, we seek a solution for Q_e by analysing the local fountain–interface interaction.

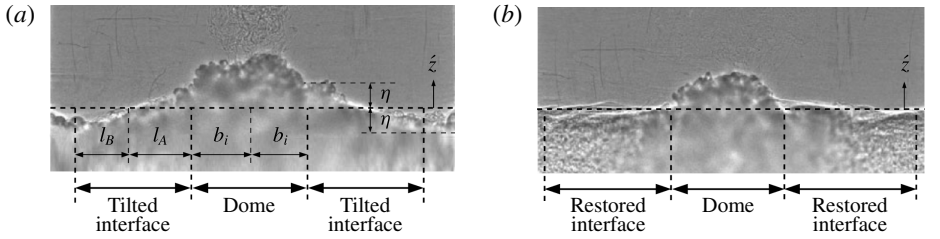

FIGURE 5. Shadowgraph images from Hunt & Coffey's (2010) experiments: (*a*) the local upward deflection of a density interface resulting from the impingement of a turbulent fountain; (*b*) the flow 15 s later when the interface has been temporarily restored back to horizontal.

2.1. *Global conservation equations*

For an incompressible flow, the volume flux Q_{P_i} supplied to the upper layer by the plume at the interface is exactly balanced by the volume flux leaving this layer, i.e. via the sum of that entrained Q_e and driven through the top opening $Q_t = Q_{f_0}$. The buoyancy flux supplied to the upper layer comprises B_P and the flux of buoyancy $g_1' Q_{P_i}$ entrained by the plume from the lower layer. The impinging fountain entrains a flux of buoyancy $g_2' Q_e$ from the upper layer and the outflow from the box expels buoyant fluid at a rate $g_2' Q_t$. Thus, for the upper layer, conservation of volume and buoyancy require, respectively,

$$Q_{P_i} = Q_e + Q_t, \quad B_P + g_1' Q_{P_i} = g_2' \left(Q_e + Q_t\right). \tag{2.3a,b}$$

Inspired by the long history of simplified models on turbulent plumes and fountains, top-hat profiles are adopted for the time-averaged horizontal variation of the vertical velocity and buoyancy of the plume and fountain. Following the classic plume theory of Morton, Taylor & Turner (1956),

$$Q_{P_i} = C_P B_P^{1/3} h^{5/3}, \quad C_P = \frac{6\alpha_P}{5}\left(\frac{9\alpha_P \pi^2}{10}\right)^{1/3}, \tag{2.4a,b}$$

where α_P is the top-hat entrainment coefficient for the plume. Following Turner (1986) we take $\alpha_P = 0.117$. As the plume is merely an artefact in the problem, in (2.4) we have neglected the effects of the secondary flow on plume entrainment. Although the secondary flow may modify the entrainment coefficient α_P, the choice of α_P does not influence the scaling of Q_e, which is the quantity of primary interest to us.

The source buoyancy flux of the fountain B_{f_0} and the buoyancy flux turbulently entrained via the impingement dome from the upper layer $g_2' Q_e$ are supplied to the lower layer. Due to entrainment into the plume, a flux of buoyancy $g_1' Q_{P_i}$ is removed from the lower layer. Thus, conservation of buoyancy for the lower layer requires

$$B_{f_0} + g_2' Q_e = g_1' Q_{P_i}. \tag{2.5}$$

Denoting b_{f_0} and w_{f_0} as the radius and vertical velocity, respectively, of the fountain at its source,

$$Q_{f_0} = \pi b_{f_0}^2 w_{f_0}, \quad B_{f_0} = -\pi g_{f_0}' b_{f_0}^2 w_{f_0}. \tag{2.6a,b}$$

The conservation equations, (2.3) and (2.5), are reduced to their simplest form by scaling the layer buoyancies on the source buoyancy $g'_{f_0} = |B_{f_0}|/Q_{f_0}$ of the fountain and scaling the interface height on the box height H. Accordingly, we introduce the dimensionless variables

$$\delta_1 = \frac{g'_1}{g'_{f_0}}, \quad \delta_2 = \frac{g'_2}{g'_{f_0}}, \quad \xi = \frac{h}{H}. \tag{2.7a–c}$$

To proceed, we substitute (2.4) into (2.3*a*) and rearrange for h. We then substitute for g'_1 from (2.5) into (2.3*b*). Non-dimensionalising the resulting equations yields closed-form solutions for the dimensionless interface height and the dimensionless layer buoyancies:

$$\xi = \left(\frac{\mathscr{L} Fr_0^{2/5}}{\psi^{1/5}}\right)(1+E)^{3/5}, \quad \delta_1 = \frac{E(\psi-1)-1}{1+E}, \quad \delta_2 = \psi - 1, \quad \text{where } E = \frac{Q_e}{Q_{f_0}}. \tag{2.8a–c}$$

The three resulting non-dimensional parameters (2.9) of our system are the buoyancy flux ratio ψ, the fountain source Froude number Fr_0 and the dimensionless radius $\mathscr{L}$ of the fountain source:

$$\psi = \frac{B_P}{|B_{f_0}|}, \quad Fr_0 = \pi^{1/4}\frac{M_{f_0}^{5/4}}{Q_{f_0}|B_{f_0}|^{1/2}}, \quad \mathscr{L} = \left(\frac{\pi^{2/5}}{C_p^{3/5}}\right)\frac{b_{f_0}}{H}. \tag{2.9a–c}$$

At this stage, $E = Q_e/Q_{f_0}$ is the single unknown dimensionless quantity. In order to determine Q_e and hence close the problem, we now model the fountain–interface interaction.

2.2. *Secondary flow in the environment*

The impingement of the fountain produces a 'local' upward deflection of the interface. To produce a local deflection, we require the radius of the impinging fountain $b_i \ll \sqrt{S}$. Although the two-layer fluid remains close to hydrostatic equilibrium, the 'tilting' of the interface indicates that the surfaces of constant pressure and constant density are no longer parallel. The action of the resulting baroclinic torque reduces the horizontal density gradients eventuating from the interfacial deflection and restores the interface back to the horizontal. The sustained forcing of the interface by the fountain gives rise to a near-continuous cycle of vertical deflections from the horizontal. This perpetual process is confirmed by several experimental studies (Kumagai 1984; Shy 1995; Hunt & Coffey 2010). Figure 5 shows shadowgraph images from Hunt & Coffey's (2010) experiments; in figure 5(*a*), the interface between two saline layers of different density is deflected upwards due to the localised impingement of a fountain from below. A short time later, the interface has been temporarily restored to its stable horizontal orientation (figure 5*b*).

When the interface tilts, (heavy) fluid of density ρ_1 within the lower layer is displaced upwards and (light) fluid of density ρ_2 within the upper layer is displaced downwards. Thence, as the baroclinic torque acts to restore the interface, the potential energy of the displaced fluids is released and a fraction of this energy is converted into kinetic energy that drives fluid motions. As a direct consequence of the near-continuous release of potential energy from the perpetual cycle of interfacial deflections, a quasi-steady secondary flow is established and maintained in the upper

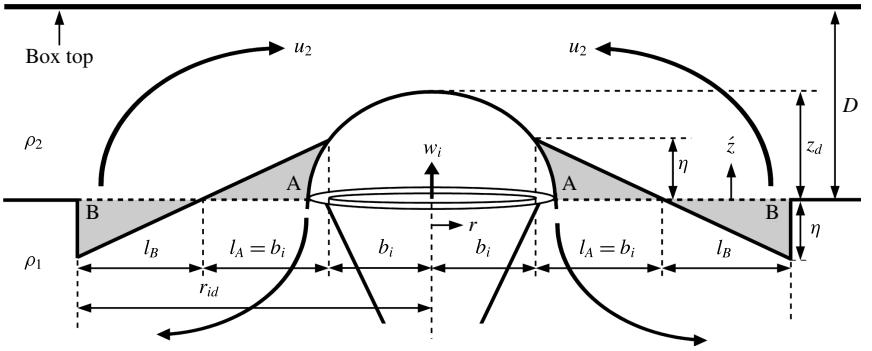

FIGURE 6. Schematic showing the modelled maximum deflection of the interface resulting from the impingement of the fountain. The position of the undisturbed interface is $\acute{z} = 0$. Due to the deflection, fluid is displaced in shaded regions A and B. Solid arrows in the upper and lower layers indicate the secondary flow induced by interfacial tilting.

and lower layers (see appendix A for arguments on why the secondary flow is quasi-steady). Crucially, therefore, fluid with non-zero velocity is entrained into the impingement dome. Ching *et al.* (1993) observed secondary flows in the environment with velocities in the upper layer of up to 30 % of the plume's vertical velocity at the interface (figure 3). Accordingly, to account for the non-zero flux of momentum entrained into the dome, we consider a time-averaged picture and seek an expression for the mean velocity u_2 of the secondary flow in the upper layer.

In a given cycle of interfacial deflection, the interface attains a maximum vertical displacement of $\acute{z} = \eta$ from its equilibrium position at $\acute{z} = 0$, as depicted in figure 6. Dense lower-layer fluid is displaced upwards above $\acute{z} = 0$ in region A and an equal volume of light upper-layer fluid is displaced downwards below $\acute{z} = 0$ in region B (of horizontal extent l_B). Guided by observations (cf. figure 5), we assume that the horizontal extent, l_A, of the upward deflection is equal to the horizontal length scale, b_i, of the forcing that produces the deflection. The deflection of the interface is thereby assumed to occur within a circular region of radius $r_{id} = b_i + l_A + l_B = 2b_i + l_B$, which we refer to as the 'zone of interfacial deflection' (the subscript '*id*' meaning 'interfacial deflection'). Whilst the deflected interface typically exhibits a relatively smoothly varying profile (figure 5*a*), the gradient of our assumed profile is discontinuous at $r = r_{id}$. Nevertheless, we will see that our model provides a simple yet effective starting point for quantifying the velocity u_2 resulting from the deflections. For the impingement of an axisymmetric fountain, the deflected regions are characterised by an annular prism whose outer radius and inner radius are $\{2b_i, b_i\}$ for region A and $\{2b_i + l_B, 2b_i\}$ for region B. Accordingly, in the displaced state

$$\frac{\pi}{2}\eta\left[(2b_i)^2 - b_i^2\right] = \frac{\pi}{2}\eta[(2b_i + l_B)^2 - (2b_i)^2]. \tag{2.10}$$

Rearranging (2.10) gives a quadratic in l_B/b_i, which has a single positive root:

$$\frac{l_B^2}{b_i^2} + 4\frac{l_B}{b_i} - 3 = 0, \quad \frac{l_B}{b_i} = (\sqrt{7} - 2) \approx 0.65. \tag{2.11a,b}$$

When the interface attains its maximum displacement ($\acute{z} = \eta$), fluid in regions A and B momentarily comes to rest. Subsequently, as the interface is restored, the displaced

fluids are set in motion. Thus, at the instant when maximum tilting occurs there is no flux of momentum into, or out of, region A. Hence, conservation of vertical momentum for this fluid volume requires

$$\rho_i Q_i w_i = \frac{3\pi}{2} b_i^2 \eta \rho \Delta g', \tag{2.12}$$

i.e. the interface is brought momentarily to rest when the upward excitation force (left-hand side) causing the interfacial deflection is balanced by the downward restoring buoyancy force (right-hand side) acting on the displaced fluid of volume $3\pi b_i^2 \eta/2$ (2.10). Here, ρ_i denotes the density of the fountain at the level of the undisturbed interface. Under the Boussinesq approximation, the maximum vertical displacement of the interface is, from (2.12),

$$\frac{\eta}{b_i} = \frac{2}{3} Fr_i^2. \tag{2.13}$$

As we shall see in § 2.3, the penetration depth of the impingement dome is $z_d/b_i = 0.94 Fr_i^2$. Evidently, the scalings of η and z_d on Fr_i are identical, which is not surprising given that both the origin of the interfacial deflection and the shallow-penetration dome is the vertical forcing by the fountain. We note that $\eta/z_d < 1$, a result one would expect on physical grounds. Moreover, our prediction that $\eta/z_d \approx 0.7$ is consistent with observations (cf. figure 5*a*).

Upon calculating the potential energy of the two-layer fluid in the displaced state PE_{dis} and the potential energy of the equilibrium state PE_{eq} (see appendix B), we find that the surplus potential energy available for conversion into kinetic energy is

$$\mathrm{APE} = \mathrm{PE}_{dis} - \mathrm{PE}_{eq} = \pi \rho \Delta g' b_i^2 \eta^2. \tag{2.14}$$

As the action of the baroclinic torque temporarily restores the tilted interface from the point of maximum deflection ($\acute{z} = \eta$) to the equilibrium position ($\acute{z} = 0$), the available potential energy (2.14) is converted into kinetic energy for driving fluid motion in the upper and lower layers primarily over the radial extent r_{id}. A flow towards the impingement dome is established within the upper layer, whereby light fluid of density ρ_2 replaces heavy fluid of density ρ_1 in region A (figure 6). We note that the hydrostatic pressure variations established by the tilting, and indeed the entrainment into the dome, induce a flow towards the dome. Similarly, a flow towards the side walls of the box is established within the lower layer, whereby fluid of density ρ_1 replaces fluid of density ρ_2 in region B. In our time-averaged conceptualisation, the mean kinetic energy of the secondary flow prevailing in the upper layer is

$$\mathrm{KE}_2 = \int_h^H \pi \rho_2 \frac{u_2^2}{2} r_{id}^2 \, \mathrm{d}z = \pi \rho_2 r_{id}^2 (H - h) \frac{u_2^2}{2}. \tag{2.15}$$

Given that we seek a local velocity for the bulk-flow-induced adjacent to the dome, in (2.15) we have calculated the kinetic energy of the flow within the region of interfacial deflection (i.e. for $r \leqslant r_{id}$). Continuous vertical oscillations of the interface typically contribute to the generation of interfacial gravity waves that extract a fraction of the potential energy released from the interfacial deflections. Some of the available potential energy may also be dissipated due to viscous effects. Thus, a fraction c of the available potential energy remains after dissipation. For simplicity, and indeed in the absence of data to support or justify a more complex energy balance, we apportion the available potential energy (after dissipation) equally between the kinetic

energies of the flows in the upper and lower layers, i.e. $\mathrm{KE}_2 = c(\mathrm{APE}/2)$. Seeking an upper-bound solution for u_2, we neglect local energy losses so that $c = 1$. Under the Boussinesq approximation, the dimensionless mean velocity $\tilde{u}_2$ of the secondary flow in the upper layer is then

$$\tilde{u}_2 = \frac{u_2}{w_i} = \frac{2}{3\sqrt{7}} cFr_i\sqrt{\lambda_i} \approx 0.25Fr_i\sqrt{\lambda_i}, \tag{2.16}$$

where the 'confinement' parameter

$$\lambda_i = \frac{b_i}{H-h}. \tag{2.17}$$

Evidently, λ_i characterises the length scale of interfacial turbulence relative to the vertical extent $(H-h)$ of the confinement. Accordingly, hereafter 'confinement' refers to 'vertical confinement'. For a given b_i and Fr_i, a relatively weak secondary flow ($\tilde{u}_2 \ll 1$) is established in the upper layer when the impingement occurs at low elevations ($h \ll H$) in a tall box such that λ_i is relatively small. In this limit, we expect our prediction of u_2 to be less reliable as the local interfacial deflections are unlikely to induce fluid motions over the depth of a relatively deep upper layer. However, we note that in the absence of confinement $\lambda_i \to 0$ and $\tilde{u}_2 \to 0$ (2.16), which is entirely consistent with the unconfined case where interfacial entrainment occurs in the absence of a secondary flow (Shrinivas & Hunt 2014).

In contrast, the secondary flow is relatively strong when the impingement occurs at high elevations in a short box such that λ_i is relatively large. In this limit, we expect our model to capture well the dynamics of the secondary flow as the interfacial deflections are likely to excite fluid motions over the full depth of a relatively shallow upper layer, as indicated in figure 3(*b*). Indeed, it is this limit that is of primary interest to us. Moreover, we will see that for previous experimental studies λ_i varies in the range $0.1 < \lambda_i < 1$, with the majority of the values of λ_i exceeding $\lambda_i = 0.3$, i.e. λ_i was relatively large for previous experiments. Given that we focus on $Fr_i \lesssim 1$, $\tilde{u}_2 \sim O(1)$ (2.16). Thus, the velocity $\tilde{u}_2$ of the secondary flow cannot be reasonably ignored. In § 3.1, we establish the range of λ_i that may be regarded as 'small' and 'large'.

2.3. *Impingement dome*

Having determined u_2, our attention turns to the volume flux Q_e of buoyant fluid, with velocity u_2, turbulently entrained from the upper layer into the axisymmetric semi-ellipsoidal impingement dome atop the incident fountain (figure 7). To model the entrainment into the dome, we employ the theoretical framework developed in Shrinivas & Hunt (2014). The entrained fluid is transported across the interface through an annulus of width $(b_d - b_i)$. Adopting top-hat profiles for the variation of the vertical downward velocity $\dot{w}_d < 0$ and density ρ_d across this annular region, conservation of volume for the impingement dome requires

$$\pi b_i^2 w_i + Q_e = \pi(b_d^2 - b_i^2)w_d, \tag{2.18}$$

where $w_d = |\dot{w}_d|$. The dome receives a flux of momentum $\pi\rho_i b_i^2 w_i^2$ from the fountain and a flux of momentum $\pi\rho_d(b_d^2 - b_i^2)w_d^2$ is transported out of the dome through the annulus. Guided by the measurements of Ching *et al.* (1993) (figure 3), we assume that the secondary flow in the vicinity of the dome boundary is horizontal.

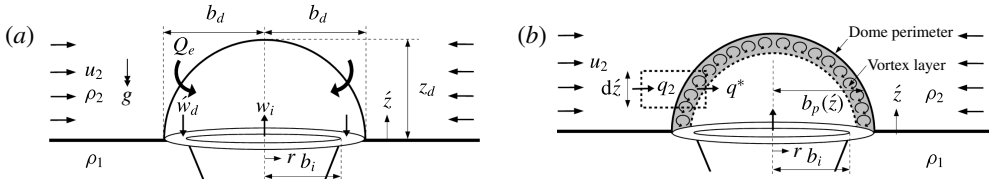

FIGURE 7. Schematic showing (*a*) the small-Fr_i axisymmetric semi-ellipsoidal impingement dome atop the impinging fountain and (*b*) the modelled vortex layer (shaded area) of the dome. In (*b*), the dashed box is the control volume considered for the inflow into the dome due to turbulent entrainment.

Accordingly, the flux of vertical momentum entrained into the dome is zero. Therefore, conservation of vertical momentum for the dome requires

$$\pi\rho_i b_i^2 w_i^2 + \pi\rho_d(b_d^2 - b_i^2)w_d^2 = \frac{2\pi}{3} b_d^2 z_d \rho_i g_i', \quad g_i' = g\left(\frac{\rho_i - \rho_2}{\rho}\right), \tag{2.19}$$

where g_i' is the mean buoyancy experienced by dense fluid within the dome of volume $2\pi b_d^2 z_d/3$. Substituting for w_d from (2.18) into (2.19) gives

$$E_i^2 + 2E_i = \frac{2}{3k^4}\frac{\hat{z}_d^5 \check{g}_i'}{Fr_i^2} - \frac{2}{3k^2}\frac{\hat{z}_d^3 \check{g}_i'}{Fr_i^2} - \frac{1}{k^2}\hat{z}_d^2, \tag{2.20}$$

for Boussinesq flows, where

$$\hat{z}_d = \frac{z_d}{b_i}, \quad k = \frac{z_d}{b_d}, \quad \check{g}_i' = \frac{g_i'}{\Delta g'} \tag{2.21a–c}$$

are the dimensionless penetration depth, the aspect ratio of the dome and the dimensionless buoyancy of the fountain at the interface, respectively. We will see (§§ 3.2, 3.3) that solutions of (2.8) are realised for fountains with source Froude numbers $Fr_0 \gg 1$ and source buoyancy flux ratios $\psi \gg 1$, i.e. the impinging fountain is highly forced at its source. For these source conditions, the fountain behaviour is jet-like over a significant fraction of the rise height, and hence its density ρ_i at the interface is comparable with ρ_1 for Boussinesq flows. Accordingly, we invoke the approximation that $\check{g}_i' \approx 1$, which considerably simplifies the analysis whilst having little effect on the solution. By considering conservation of buoyancy for the dome, we find that our approximation $\check{g}_i = 1$ leads to a marginal overprediction (by no more than 4 %) of Q_e (see appendix C).

To close the problem, it is necessary to describe the mechanism by which external fluid is entrained into the dome. The representation of turbulence, necessary to close the problem mathematically, forms the cornerstone of the mechanistic entrainment model developed by Shrinivas & Hunt (2014). Shy (1995) and Cotel *et al.* (1997) identified that the interaction between the incident vorticity within the impinging flow and the baroclinic vorticity generated at the interface, due to its tilting, results in the formation of strong persistent vortices within a relatively thin layer around the perimeter of the dome. These rotational motions are predominantly responsible for the entrainment into the dome. By modelling this peripheral region of strong vorticity as a finite-thickness vortex layer (the shaded region of the schematic of figure 7*b*),

Shrinivas & Hunt (2014) related the generation of baroclinic vorticity to the resulting mean entrainment velocity u_e and showed that

$$u_e = \alpha_d \sqrt{2\Delta g'(z_d - \acute{z})}, \tag{2.22}$$

i.e. the entrainment velocity is proportional to a local buoyancy velocity. Here, α_d is an entrainment coefficient, an appropriate value for which is $\alpha_d = 0.1$ (Turner 1986).

To account for the horizontal momentum ($\propto u_2$) of the fluid entrained from the upper layer, we consider a control volume of height $\mathrm{d}\acute{z}$ around the dome perimeter (figure 7*b*). Owing to the secondary flow, a volume flux q_2 per unit height with fluid of velocity u_2 enters the control volume. A volume flux q^* per unit height leaves the control volume and enters the dome at velocity u^*. Thus, conservation of horizontal momentum for the flow near the dome boundary requires

$$\rho^* q^* u^* \,\mathrm{d}\acute{z} - \rho_2 q_2 u_2 \,\mathrm{d}\acute{z} = F_e, \tag{2.23}$$

where F_e denotes the inertial force of the peripheral energy-containing vortices that drive entrainment into the dome and ρ^* denotes the density of the fluid entering the vortex layer. Over a vertical extent $\mathrm{d}\acute{z}$ of the vortex layer, a volume $\mathrm{d}V_e$ of external fluid is engulfed at velocity u_e in a time $\mathrm{d}t$. Therefore, the inertial force associated with the energy-containing vortices that gives rise to and maintains the steady inflow into the dome is

$$F_e = \rho_2 u_e \,\mathrm{d}V_e/\mathrm{d}t. \tag{2.24}$$

Under the Boussinesq approximation, substituting for F_e (2.24) into (2.23) and given that conservation of volume for the steady flow requires $q_2 \,\mathrm{d}\acute{z} = q_e \,\mathrm{d}\acute{z} = \mathrm{d}V_e/\mathrm{d}t$, we obtain

$$u^* = u_e + u_2, \tag{2.25}$$

i.e. the mean horizontal inflow velocity u^* across the boundary between the turbulent flow and the external environment is given by the sum of the entrainment velocity of the peripheral vortices and the velocity of the secondary flow in the upper layer. To further support this entrainment formulation, we may draw a direct analogy between plumes rising in a weak crossflow and our dome in the midst of a predominantly horizontal secondary flow. The net entrainment into a plume rising in a crossflow is the sum of two parts, namely, the entrainment driven by the vertical shear and the entrainment of the crossflow (Hoult & Weil 1972; Lee & Chu 1979; Devenish *et al.* 2010). Similarly, the net entrainment into the dome in the presence of a secondary flow comprises two components, namely, the entrainment driven by baroclinic vortices and the entrainment of the secondary flow. Thus, (2.25) is consistent with well-established entrainment models for plumes in a crossflow.

The total volume flux entrained into the dome over the height $0 \leqslant \acute{z} \leqslant z_d$ is

$$Q_e = \int_0^{z_d} 2\pi b_p u^* \,\mathrm{d}\acute{z} = \int_0^{z_d} 2\pi b_p (u_e + u_2) \,\mathrm{d}\acute{z}, \tag{2.26}$$

where b_p is the radius of the dome at height $\acute{z}$. The dome perimeter is the semi-ellipse:

$$\frac{b_p^2(\acute{z})}{b_d^2} + \frac{\acute{z}^2}{z_d^2} = 1, \quad \text{for } 0 \leqslant \acute{z} \leqslant z_d. \tag{2.27}$$

Substituting for u_2 (2.16), u_e (2.22) and b_p (2.27) into (2.26) gives

$$Q_e = \pi C b_d \sqrt{\Delta g' z_d^3}^{3/2} + \frac{\pi^2}{2} b_d z_d u_2, \quad C = \frac{4\alpha_d\sqrt{2}}{15}(8\sqrt{2}-7). \tag{2.28a,b}$$

To complete our solution we require the penetration depth z_d of the dome. For the unconfined case, wherein interfacial entrainment occurs in the absence of a secondary flow (i.e. $\tilde{u}_2 \to 0$ as $\lambda_i \to 0$), Shrinivas & Hunt (2014) considered conservation of energy for the dome and showed that

$$\hat{z}_d = \frac{z_d}{b_i} = BFr_i^2, \quad B = 0.94. \tag{2.29}$$

For the confined problem of interest here, entrainment of fluid into the dome results in an inflow of kinetic energy $\propto u_2^2$ and potential energy $\propto \Delta g' z_d$. Whilst both can be accounted for in the energy budget, an elegant approximation becomes evident on examining the relative magnitudes of the kinetic and potential energies entrained. Given that $z_d/b_i \propto Fr_i^2$, the ratio of the entrained energies is $u_2^2/(\Delta g' z_d) \propto u_2^2/w_i^2$. Noting that $u_2^2/w_i^2 \ll 1$ (2.16) for the range of $\{Fr_i, \lambda_i\}$ considered, the kinetic energy entrained into the dome is relatively small and thus may reasonably be neglected. Hence, the secondary flow has a relatively minor influence on the energy budget for the dome. Thus, to a good approximation, the penetration depth of the confined dome is given by (2.29).

With the problem fully closed, we substitute for u_2 (2.16) and z_d (2.29) into (2.28). The resulting expression is rearranged for the aspect ratio k and substituted into (2.20). This yields a cubic in E_i as a function of the interfacial Froude number and the confinement parameter:

$$E_i^3 - a_1 E_i - a_2 = 0, \tag{2.30}$$

where

$$a_1 = \frac{3a_3^2}{2B}\left(1 + \frac{2B}{3} + a_3^2\right), \quad a_2 = \frac{3}{B}a_3^4, \quad a_3 = B^{3/2}CFr_i^2 + \frac{\pi B}{8}\lambda_i^{1/2}Fr_i^3. \tag{2.31a–c}$$

This cubic has a single positive root, namely

$$E_i = \left\{\frac{a_2}{2} + \sqrt{\left(\frac{a_2}{2}\right)^2 - \left(\frac{a_1}{3}\right)^3}\right\}^{1/3} + \left\{\frac{a_2}{2} - \sqrt{\left(\frac{a_2}{2}\right)^2 - \left(\frac{a_1}{3}\right)^3}\right\}^{1/3}. \tag{2.32}$$

For $Fr_i < 1$ and $\lambda_i < 1$, a two-step procedure (see appendix D) reduces (2.32) to the simple analytic solution

$$E_i = \underbrace{AFr_i^2}_{\substack{\text{unconfined}\\ \text{component}}} + \underbrace{K\sqrt{\lambda_i}Fr_i^3}_{\substack{\text{confined}\\ \text{component}}}, \tag{2.33}$$

which closely approximates the full solution. In (2.33),

$$A = BC\sqrt{B + \frac{3}{2}} \approx 0.24 \quad \text{and} \quad K = \frac{\pi A}{8\sqrt{B}C} \approx 0.60. \tag{2.34a,b}$$

The first term of (2.33) is the contribution to the total volume flux into the dome due to entrainment driven by peripheral vortices and the second term is the volume flux into the dome due to entrainment of the secondary flow.

When interfacial entrainment occurs in an unconfined environment, $\lambda_i \to 0$ and $\tilde{u}_2 \to 0$ (2.16). In this limit $E_i = E_i(Fr_i)$ and we recover our solution $E_i = AFr_i^2$ for unconfined entrainment (Shrinivas & Hunt 2014). When interfacial entrainment occurs within the confines of a box so that $\lambda_i > 0$, a secondary flow persists ($\tilde{u}_2 > 0$) and $E_i = E_i(Fr_i, \lambda_i)$. Thus, the second term of (2.33) solely accounts for the role of confinement. To quantify the influence of confinement on E_i, we consider the total entrainment flux E_i relative to the entrainment flux in the absence of confinement (i.e. the unconfined component in (2.33)). Accordingly, we introduce the ratio

$$\phi = \frac{AFr_i^2 + E_{i,c}}{AFr_i^2}, \quad \text{where } E_{i,c} = K\sqrt{\lambda_i} Fr_i^3 \tag{2.35}$$

is the rate of entrainment of the secondary flow (the subscript 'c' meaning 'confined'). When $\phi \sim 1$, the contribution of $E_{i,c}$ to E_i is small and box confinement does not significantly influence the rate of interfacial entrainment. When $\phi \gg 1$, $E_{i,c}$ provides a significant contribution to E_i, and hence confinement plays an instrumental role in increasing the total entrainment flux E_i.

2.4. *Impinging fountain*

To predict Fr_i and λ_i, it is necessary to model the fountain. Assuming that the downflow of the fountain is fully incorporated into the lower layer, conservation of volume flux ($\pi b_f^2 w_f$), momentum flux ($\pi b_f^2 w_f^2$) and buoyancy flux ($-\pi b_f^2 w_f g_f'$) for the fountain upflow requires (Morton *et al.* 1956)

$$\frac{\mathrm{d}}{\mathrm{d}z}(\pi b_f^2 w_f) = 2\pi\alpha_f b_f w_f, \quad \frac{\mathrm{d}}{\mathrm{d}z}(\pi b_f^2 w_f^2) = -\pi b_f^2 g_f', \quad \frac{\mathrm{d}}{\mathrm{d}z}(\pi b_f^2 w_f g_f') = 0, \tag{2.36a–c}$$

where α_f is the top-hat entrainment coefficient for the fountain. Following Kaye & Hunt (2006), we take $\alpha_f = 0.085$. Given that the fountain behaviour is jet-like for the majority of its rise height, the vertical velocity w_f of the fountain is large compared with the velocity of the secondary flow in the lower layer. Therefore, it is reasonable to assume that entrainment into the fountain is not significantly influenced by the secondary flow in the lower layer. Whilst the secondary flow may modify the entrainment coefficient α_f, it is reassuring that the choice of α_f does not influence the scaling of E_i, the quantity of primary interest to us.

Scaling quantities of interest on their values at the fountain source, we seek the vertical variation of the dimensionless radius $\beta_f = b_f/b_{f_0}$, vertical velocity $\omega_f = w_f/w_{f_0}$ and local Froude number $Fr_f = w_f/\sqrt{b_f g_f'}$ of the fountain. The non-dimensional governing equations for the fountain are

$$\frac{\mathrm{d}\beta_f}{\mathrm{d}\mathscr{Z}} = \frac{5}{3}\left(1 + \frac{1}{4\alpha_f Fr_f^2}\right), \quad \frac{\mathrm{d}\omega_f}{\mathrm{d}\mathscr{Z}} = -\frac{5}{3}\frac{\omega_f}{\beta_f}\left(1 + \frac{1}{2\alpha_f Fr_f^2}\right), \quad \frac{\mathrm{d}Fr_f}{\mathrm{d}\mathscr{Z}} = -\frac{5}{3}\frac{Fr_f}{\beta_f}\left(1 + \frac{5}{8\alpha_f Fr_f^2}\right), \tag{2.37a–c}$$

where $\mathscr{Z} = (6\alpha_f/5)z/b_{f_0}$. The source conditions of the fountain are $\beta_f(\mathscr{Z} = 0) = 1$, $\omega_f(\mathscr{Z} = 0) = 1$ and $Fr_f(\mathscr{Z} = 0) = Fr_0$.

The non-dimensional parameters of our system (2.9) are the source Froude number Fr_0 of the fountain, the buoyancy flux ratio ψ and the fountain source radius $\mathscr{L}$. For a given $\{Fr_0, \psi, \mathscr{L}\}$, solutions were obtained using an iterative procedure. First, by making an initial estimate of $E = Q_e/Q_{f_0}$, the interface position (ξ) and mean

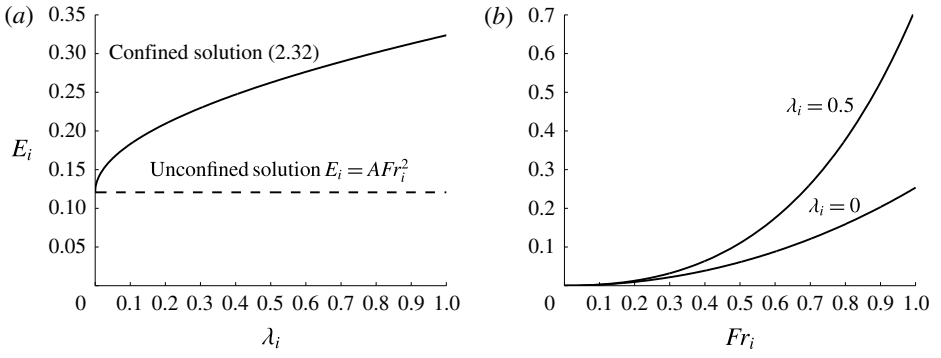

FIGURE 8. Dimensionless entrainment flux E_i across the interface: (a) as a function of the confinement parameter λ_i for $Fr_i = 0.7$ and (b) as a function of the interfacial Froude number Fr_i for $\lambda_i = \{0, 0.5\}$.

layer buoyancies (δ_1, δ_2) were calculated from (2.8a–c). Subsequently, the fountain equations (2.37) were solved to obtain the dimensionless vertical velocity ω_i and dimensionless radius β_i of the fountain at the interface. The interfacial Froude number and the confinement parameter were determined from

$$Fr_i = Fr_0 \frac{\omega_i}{\sqrt{\beta_i\,(\delta_2 - \delta_1)}}, \quad \lambda_i = \left(\frac{\mathscr{L} C_p^{3/5}}{\pi^{2/5}}\right) \frac{\beta_i}{1-\xi}. \tag{2.38a,b}$$

We then calculated the dimensionless entrainment flux E_i (2.33) and re-estimated $E = E_i \beta_i^2 \omega_i$, the interface position and the layer buoyancies. This procedure was repeated until E_i, ξ, δ_1 and δ_2 converged to fixed values.

3. Model predictions and analysis of results

3.1. *Power laws for unconfined and confined entrainment*

As an illustrative example of the role of confinement, figure 8(a) plots E_i as a function of λ_i for $Fr_i = 0.7$. Also plotted is the power law $E_i = AFr_i^2$ for unconfined interfacial entrainment. As λ_i increases, and thus the confinement is enhanced, the velocity $\tilde{u}_2 (\propto \sqrt{\lambda_i})$ of the secondary flow increases (see § 3.3 for a further discussion on the role of λ_i). Therefore, the rate of entrainment $E_{i,c} (\propto \tilde{u}_2)$ of the secondary flow and hence E_i increase with λ_i (figure 8a). Notably, when the radius of the impinging fountain equals the depth of the upper layer (i.e. $\lambda_i = 1$), E_i exceeds the rate of interfacial entrainment in an unconfined environment by a factor of three.

Figure 8(b) plots E_i as a function of Fr_i for $\lambda_i = \{0, 0.5\}$ and further emphasises the disparities between entrainment in unconfined and confined environments. As Fr_i increases, and thus the vertical forcing of the interface is strengthened, larger deflections η ($\propto Fr_i^2$) are produced. Hence, for $\lambda_i > 0$ a greater amount of potential energy is released and converted into kinetic energy of the secondary flow. Therefore, $\tilde{u}_2$ and E_i increase with Fr_i (figure 8b). Significantly, when the diameter ($2b_i$) of the impinging fountain equals the upper-layer depth (i.e. $\lambda_i = 0.5$), doubling Fr_i from $Fr_i = 0.5$ to $Fr_i = 1$ gives rise to a sevenfold increase in E_i; this compares with a fourfold increase in the unconfined case.

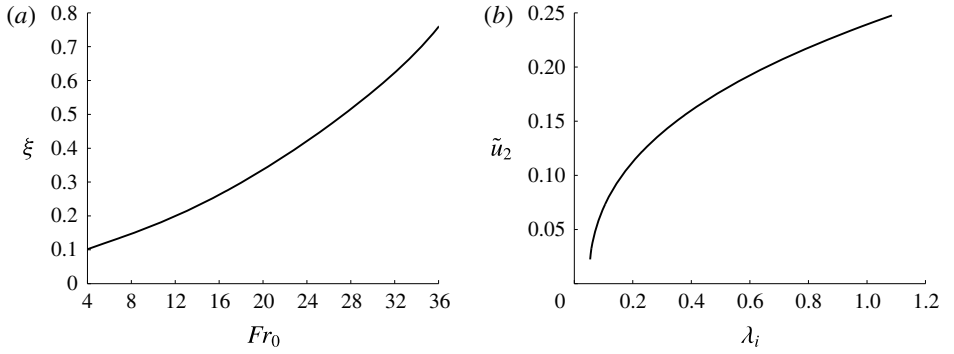

FIGURE 9. (*a*) Interface height ξ against the source Froude number Fr_0 of the fountain and (*b*) velocity $\tilde{u}_2$ of secondary flow against the confinement parameter λ_i for buoyancy flux ratio $\psi = 25$ and fountain source radius $\mathscr{L} = 0.1$.

Crucially, the scaling of E_i on Fr_i is determined by λ_i. From (2.33), our entrainment law follows

$$E_i \propto \begin{cases} Fr_i^2 & \text{for } \lambda_i \ll \lambda_{i,c}, \\ Fr_i^3 & \text{for } \lambda_i \gg \lambda_{i,c}, \end{cases} \quad \lambda_{i,c} = \frac{64BC^2}{\pi^2 Fr_i^2}. \tag{3.1}$$

In other words, when $\lambda_i \ll \lambda_{i,c}$, the secondary flow is sufficiently weak such that the contribution of $E_{i,c}$ to E_i is small, and thus E_i is quadratic in Fr_i as per 'unconfined' entrainment (Shrinivas & Hunt 2014). When $\lambda_i \gg \lambda_{i,c}$, the secondary flow is sufficiently strong such that $E_{i,c}$ provides the dominant contribution to E_i and thus, E_i is cubic in Fr_i (2.33). We refer to interfacial entrainment in these small-λ_i and large-λ_i limits as weakly confined and strongly confined, respectively.

This result provides a plausible physical explanation for why some experimental studies support a $E_i \propto Fr_i^2$ power law, whereas others report $E_i \propto Fr_i^3$. Our model (3.1) indicates that measurements of E_i following a cubic power law (Baines 1975; Coffey & Hunt 2010) may have been influenced by a secondary flow owing to relatively large values of λ_i. Inferring values of λ_i from previous works, we find that for the experiments of Coffey & Hunt (2010), λ_i was as large as unity, as discussed in § 3.3. Conversely, measurements of E_i supporting a quadratic power law (Cardoso & Woods 1993; Ching *et al.* 1993) were not significantly influenced by a secondary flow as λ_i was sufficiently small. Indeed, for the experiments of Ching *et al.* (1993), a value of $\lambda_i = 0.2$ was never exceeded. We will see (§ 3.3) that for previous studies, λ_i exhibits wide variation, spanning the range $0.1 < \lambda_i < 1$. Hence, these studies capture E_i not only within the weakly confined and strongly confined regimes, but also in the transitional regime where comparable contributions from the quadratic and cubic components are expected.

3.2. *Entrainment for varying Fr_i and λ_i*

Thus far, we have focused on entrainment for constant Fr_i or constant λ_i (figure 8). The difficulty in achieving this in practice is exemplified by the significant variation of Fr_i and λ_i in previous experiments (see § 3.3). To examine E_i when both Fr_i and λ_i vary, we increase the source Froude number Fr_0 of the fountain, whilst holding the source radius $\mathscr{L}$ and buoyancy flux ratio ψ constant. As this produces more energetic interfacial impingements, the rate of entrainment (E_i) of fluid from the upper layer increases and hence the interface height ξ increases (figure 9*a*). Consequently, the

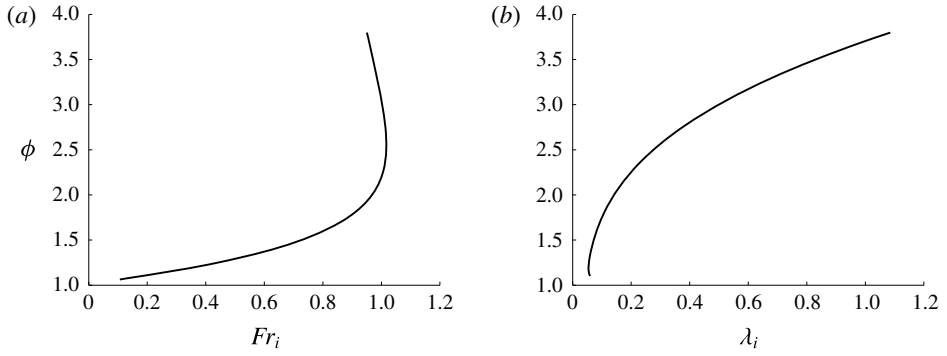

FIGURE 10. Entrainment flux ratio ϕ (2.35): (a) against the interfacial Froude number Fr_i and (b) against the confinement parameter λ_i for source buoyancy flux ratio $\psi = 25$ and fountain source radius $\mathscr{L} = 0.1$.

radius β_i of the fountain at the interface increases. Therefore, increasing Fr_0 results in larger values of $\lambda_i \propto \beta_i/(1-\xi)$. Enhancing the confinement in this way gives rise to stronger secondary flows, i.e. $\tilde{u}_2$ increases with λ_i, as shown in figure 9(b). Notably, u_2 is approximately 25 % of the fountain's vertical velocity w_i at the interface when $\lambda_i \sim 1$.

Figures 10(a) and 10(b) plot the entrainment flux ratio ϕ (2.35) against Fr_i and λ_i, respectively. Two limiting cases can be identified: one in which Fr_i and λ_i are small and a second in which Fr_i and λ_i are large. For $Fr_i \ll 1$ a weak forcing of the interface by the fountain produces relatively small deflections as $\eta \propto Fr_i^2$, and for $\lambda_i \ll 1$ the zone of interfacial deflection ($r_{id} \propto b_i$) is small compared with the depth of the upper layer, $r_{id} \ll D$. Thus, a relatively small amount of potential energy ($\sim b_i^2\eta^2$) is released from the deflections and converted into kinetic energy of a relatively large mass of upper-layer fluid. As a result, the secondary flow is weak ($\tilde{u}_2 \ll 1$), and hence the rate of entrainment $E_{i,c}$ of the secondary flow provides only a small contribution to E_i. For example, $\phi \sim 1$ when $\{Fr_i, \lambda_i\} \ll 1$ (figure 10). When Fr_i and λ_i are both large, the vertical excursions of the interface are relatively large (η is comparable with b_i) and the zone of deflection is comparable with the upper-layer depth. Thus, a significant amount of potential energy is released and converted into kinetic energy of a relatively shallow mass of upper-layer fluid. As a result, the secondary flow is strong and hence, $E_{i,c}$ provides a significant contribution to the total entrainment flux E_i. For example, $\phi \approx 4$ when $\{Fr_i, \lambda_i\} \sim 1$, i.e. with identical forcing, the entrainment flux in the confined environment exceeds that in an unconfined environment by a factor of almost four (figure 10).

3.3. *Confinement in previous experimental studies*

Figure 11 plots contours of constant E_i in $\{\lambda_i, Fr_i\}$ space, thereby encompassing the dynamics of interfacial entrainment in a confined environment. For a given Fr_i, E_i can vary by up to 80 % depending on λ_i. For example with $Fr_i = 0.7$, $E_i = 0.18$ when $\lambda_i = 0.1$, whereas $E_i = 0.32$ when $\lambda_i = 0.8$. Given that λ_i plays an instrumental role in the entrainment dynamics, it is informative to examine the confinement in previous experimental studies.

A wide range of box geometries have been used in experiments to measure E_i, with the box height H differing by more than a factor of two: see table 1. Accordingly,

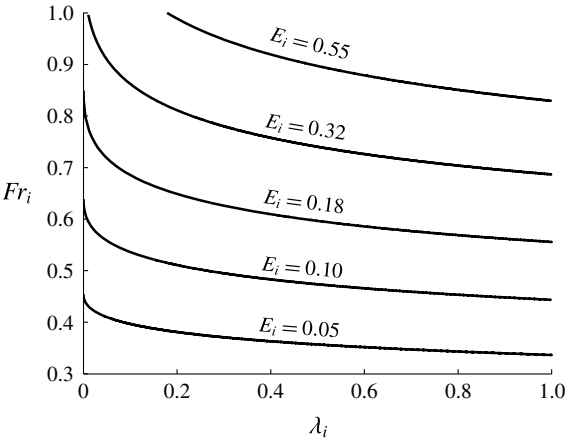

FIGURE 11. Contours of constant entrainment flux E_i in $\{\lambda_i, Fr_i\}$ space.

Researcher(s)	H (cm)	b_{f_0} (cm)	$\mathscr{L} \propto b_{f_0}/H$ (2.9)
Lin & Linden (2005)	23, 25	1.27	0.216, 0.259
Baines (1975)	30	0.5	0.085
Cardoso & Woods (1993)	30, 44	0.7	0.081, 0.119
Coffey & Hunt (2010)	30	1.5	0.255
Kumagai (1984)	37	0.5	0.069
Baines *et al.* (1993)	50	0.16	0.016

TABLE 1. Examples of the box height H, source radius b_{f_0} and dimensionless source radius $\mathscr{L}$ used in previous experimental studies.

it is instructive to examine the effect of the vertical extent H of the confinement on E_i. To this end, we vary the box height H for constant $\{b_{f_0}, Fr_0, \psi\}$, equivalent to varying $\mathscr{L} \propto b_{f_0}/H$, and calculate E_i. Figure 12 plots the entrainment flux ratio ϕ against $\mathscr{L}$. The values of $\mathscr{L}$ we consider span those of the experimental studies (table 1). Reducing H (i.e. increasing $\mathscr{L}$) strengthens the confinement and hence results in stronger secondary flows. Consequently, the rate of entrainment $E_{i,c}$ of the secondary flow increases, and thus ϕ increases with $\mathscr{L}$. For a typical source radius of $b_{f_0} = 0.6$ cm, the dashed lines in figure 12 indicate the values of ϕ corresponding to the minimum and maximum box heights used in experiment (table 1). Evidently, the enhancement of E_i due to the confinement increases by more than 50 % when the box height is decreased from $H = 50$ cm to $H = 23$ cm.

These results highlight that confinement has a significant effect on the strength of the secondary flow and thus on the entrainment flux. Of course, this variation is entirely unwanted from a practical perspective as experiments have sought to determine a universal entrainment law.

To establish whether the role of confinement can shed new light on the significant spread in the existing measurements of E_i (figure 2), figure 13 plots λ_i for the experiments of Kumagai (1984), Lin & Linden (2005) and Coffey & Hunt (2010) in $\{Fr_i, \lambda_i\}$ space. We note that Baines (1975) does not provide sufficient information to calculate λ_i for his experiments. Evidently, the experimental values of λ_i vary by up to an order of magnitude for a given Fr_i. Notably, the range of experimental

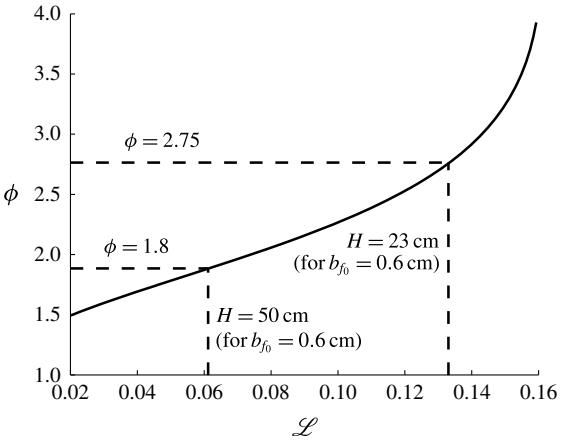

FIGURE 12. Entrainment flux ratio ϕ against dimensionless source radius $\mathscr{L}$ for source Froude number $Fr_0 = 20$ and buoyancy flux ratio $\psi = 10$. The dashed lines indicate $\phi = \{2.75, 1.8\}$ for box height $H = \{23, 50\}$ cm and source radius $b_{f_0} = 0.6$ cm.

values of λ_i ($0.1 < \lambda_i < 1$) corresponds to the range of values of λ_i predicted by our model (figure 10*b*). Moreover, there is no systematic variation of λ_i with Fr_i, thus affirming that λ_i is an independent parameter. Based on this evidence and given that the influence of λ_i on E_i has not been previously considered, it is plausible and indeed we assert that the spread in the existing data of E_i is attributed, at least in part, to the dependence of E_i on λ_i. To reinforce this assertion, also shown in figure 13 are our theoretical curves of constant $\phi = \{1.2, 4\}$. Clearly, almost all the data points lie within the shaded region bounded by these curves. In other words, we predict that for the majority of existing measurements, at least 20 % of E_i may be attributed to the rate of entrainment $E_{i,c}$ of the secondary flow, and that for strongly confined flows, the entrainment flux inferred from measurements is increased by a factor of four over that which may be expected for truly unconfined interfacial entrainment. This is compelling evidence that previous measurements have been influenced by a secondary flow and that the disparities in E_i are likely to be associated with variations in λ_i.

Baines (1975), Kumagai (1984) and Coffey & Hunt (2010) inferred E_i by tracking the position of a moving interface and, as a consequence, λ_i was time-dependent in their experiments. By using a wide tank, Ching *et al.* (1993) measured the entrainment rate before the interfacial gravity current reached the side boundaries. Thus, the interface position and λ_i were invariant for the duration of interest. It is therefore unsurprising that their measurements of the entrainment rate exhibit considerably less scatter than the data sets of Baines (1975) and Kumagai (1984), for which λ_i differs by almost an order of magnitude (figure 13).

3.4. *Implications for the design of an experiment*

It is not immediately clear for a given experiment (or indeed from the wealth of previous measurements) how the individual components of E_i (2.33) may be accurately determined. What is clear is that in search of a universal law it is the entrainment flux in the absence of confinement that has been, and arguably remains, the true goal. Our analysis raises the question of what is an appropriate box height H for measuring the

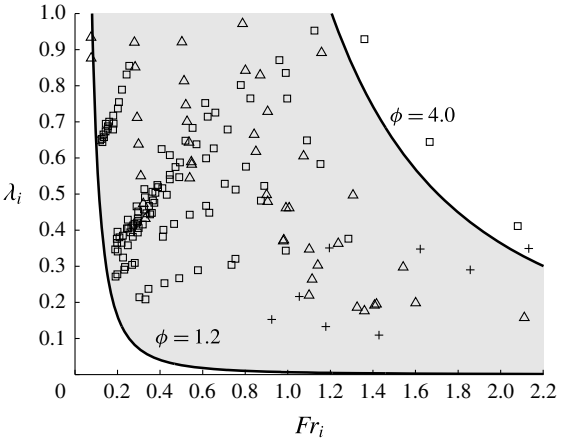

FIGURE 13. Confinement parameter λ_i against the interfacial Froude number Fr_i for the experiments of Kumagai (1984) (□), Lin & Linden (2005) (+) and Coffey & Hunt (2010) (△). Solid lines are our theoretical curves of constant entrainment flux ratio $\phi = \{1.2, 4\}$.

entrainment flux. As a secondary flow persists for $H > 0$, the influence of confinement on E_i is inexorable. However, through careful selection of the box height, it is possible to tailor the contribution of $E_{i,c}$ to E_i in an experiment so that $\phi = (AFr_i^2 + E_{i,c})/AFr_i^2$ does not exceed an acceptable threshold, ϕ_T. Based on the accuracy to which E_i is measured, experimentalists can specify ϕ_T. By ensuring that $\phi < \phi_T$, the effect of confinement on E_i can, in principle, be restricted solely to the realms of experimental uncertainty.

With a view to guiding future experiments, we seek the box height required to achieve a given $\phi = \phi_T$. While the plan area S of the box is needed to fully define the geometry, its precise value is not of concern, and implicit in the following discussion is that S is sufficiently large that both the plume and fountain are free to entrain and their sources sufficiently well separated that they may be considered to be non-interacting. Moreover, the sources are sufficiently small in area that they approximate to localised sources (e.g. $b_{f_0} \ll h$). As the fountain exhibits jet-like behaviour below the interface (see § 2.3), its radius scales approximately linearly with height (Kaye & Hunt 2006), and hence we take $b_i = c_1 h$, where c_1 is a constant. Recalling that $\lambda_i = b_i/(H - h)$, we substitute for b_i into (2.35) and rearrange for h/H to give

$$\left(\frac{h}{H}\right)_{design} = \left\{1 + \frac{c_1 K^2}{A^2}\frac{Fr_i^2}{(1-\phi_T)^2}\right\}^{-1}. \tag{3.2}$$

Taking $c_1 = 0.17$ (Mizushina *et al.* 1982), figure 14 plots $(h/H)_{design}$ (3.2) as a function of Fr_i for $\phi_T = \{1.2, 1.5, 2.0, 2.5\}$. The region beneath a given curve of constant ϕ_T encompasses the values of $(h/H)_{design}$ for which $\phi < \phi_T$. Hence, for a given interface position h, figure 14 indicates the box height H required to limit the influence of the confinement on E_i to $\phi = \phi_T$. For example, if the interface is established 12 cm above the base of the box and $Fr_i = 0.3$, we would require $H > 47$ cm to restrict the rate of entrainment $E_{i,c}$ of the secondary flow to no more than 20 % of E_i. Lower box heights could be used, but with the penalty of higher thresholds ϕ_T.

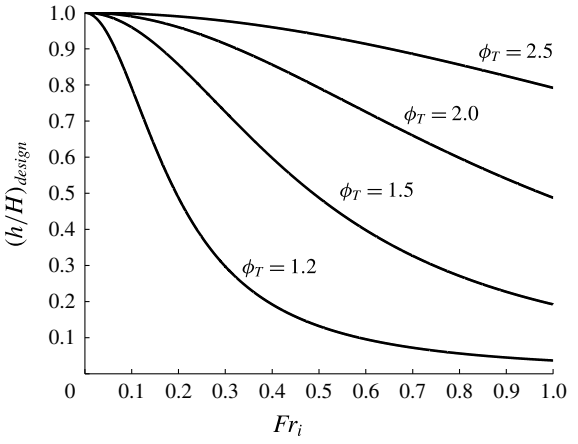

FIGURE 14. Interface height h scaled on box height H as a function of Fr_i for a constant entrainment flux ratio $\phi_T = \{1.2, 1.5, 2.0, 2.5\}$.

3.5. *Summary of key modelling assumptions*

Guided by previous experimental results and observations, a number of key modelling assumptions and simplifications have been made and these are as follows.

(i) The interfacial deflections occur within a circular region of finite radius.
(ii) The fountain, the dome and the plume occupy only a small fraction of the total volume of the box, so we may ignore the potential energies contained in these regions.
(iii) Interfacial deflections induce a flow predominantly within the zone of interfacial deflection.
(iv) Energy losses associated with the generation of interfacial waves and the energy dissipated due to viscous effects may be neglected in our analysis of the secondary flow.
(v) Persistent baroclinic vortices around the periphery of the dome are primarily responsible for entrainment into the dome.
(vi) The entrainment coefficients for the plume and the fountain are not significantly influenced by the secondary flow in the lower layer.
(vii) The available potential energy is apportioned equally between the kinetic energies of the secondary flows in the upper and lower layers.

Whilst the interfacial Froude number and the confinement parameter are instrumental in determining the entrainment flux across the interface, their values here are not specified *a priori* but span the range $0.1 \lesssim \lambda_i \lesssim 1$, $0.1 \lesssim Fr_i \lesssim 1.4$ as a consequence of the system we consider (see figures 10 and 13).

4. Conclusions

Over the last five decades, a host of experimental studies have sought to determine the dimensionless volume flux E_i turbulently entrained across a stable density interface. A wider understanding of this problem has been shrouded by the significant spread in the measurements of E_i and by the conflicting power laws describing its dependence on the interfacial Froude number Fr_i. Whilst all experiments have been conducted,

by necessity, within the confines of a (transparent) box or visual tank, the effects of confinement on interfacial entrainment have not been previously examined. Seeking to establish the role of confinement, we theoretically examined turbulent entrainment across an interface separating two uniform fluid masses within a box. Complexities associated with the time-dependent coupling between E_i and the growth of a stratified intermediate layer were overcome by considering the steady two-layer stratification established by a turbulent plume and a turbulent fountain rising from the base of the box. The plume maintains the buoyant upper layer and the localised impingement of the fountain with the interface drives entrainment of fluid from the upper layer into the lower layer via an interfacial dome.

Guided by previous experimental studies, we developed a model describing the dynamics of fountain–interface interaction and the steady secondary flow in the environment that is induced and maintained by the perpetual cycle of interfacial deflections. We deduced that besides Fr_i, E_i is dependent on a confinement parameter λ_i which characterises the length scale of interfacial turbulence relative to the depth of the upper layer. For small λ_i, a weak secondary flow has little influence on E_i which is governed by a quadratic power law $E_i \propto Fr_i^2$. For large λ_i, however, E_i is significantly influenced by a strong secondary flow and is governed by a cubic power law $E_i \propto Fr_i^3$. By establishing the range of λ_i that may be regarded as small and large, we classified the dynamics of confined interfacial entrainment into the weakly confined and strongly confined regimes.

Crucially, we established that a secondary flow persists for all box heights. Therefore, the effect of box confinement on E_i is an inescapable feature of laboratory experiments. We showed that for previous experiments, λ_i varies in the range $0.1 < \lambda_i < 1$. A key result from our model is that depending on λ_i, E_i can vary by up to an order of magnitude for a given Fr_i. Thus, the modification of E_i due to the confinement provides a plausible physical explanation for the wide disparities evident in the existing data. Based on our model, we suggest that the effects of confinement on E_i can be minimised by designing experimental configurations that satisfy $\lambda_i \ll 0.16 Fr_i^{-2}$.

For unsteady experiments (e.g. Kumagai 1984) wherein E_i is inferred by tracking the position of a moving interface, λ_i varies significantly with time, thereby compounding the inherent challenges associated with the pursuit of a universal relationship between E_i and Fr_i. To overcome this complexity, one could examine interfacial entrainment in a box whose width far exceeds its height. Measurements of E_i can then be made prior to the interfacial gravity current reaching the side walls so that the interface position and λ_i remain constant. A second option is to consider a steady system. To this end, the steady two-layer stratification established by a plume and a fountain, as considered in this paper, provides a convenient means of measuring E_i for a given λ_i. With a view to guiding future experiments, we established (figure 14) box geometries which enable the contribution of confinement to the total entrainment flux to be bounded.

Our complementary studies of unconfined (Shrinivas & Hunt 2014) and confined (herein) interfacial entrainment elucidate the key physics that underpins the entrainment law $E_i \propto Fr_i^n$. We have shown that $n = 1$ for large Fr_i, $n = 2$ for small Fr_i and $n = 3$ for large λ_i. The results and recommendations stemming from our investigation of confined entrainment may enable future studies to account for, or minimise, the effects of confinement in their experiments or numerical work. Nevertheless, the dependence of E_i on the confinement throws into question and challenges the notion of a universal entrainment law.

Acknowledgements

The authors are grateful for the comments of anonymous referees.

Appendix A. Steadiness of the secondary flow

Linden (1974) and Shy (1995) showed that the time scale associated with the displacement of the interface is $T_{dis} \propto \sqrt{b_i/\Delta g'}$. Prior to reaching the dome boundary, the secondary flow in the upper layer develops over the length scale $l_A + l_B$ (figure 6). Given that this flow is buoyancy-driven and is established within the zone of interfacial deflection of radial extent r_{id}, its characteristic velocity scale is the buoyancy velocity $\sqrt{r_{id}\Delta g'}$. Noting that $l_A + l_B \approx 1.65 b_i$ and $r_{id} = 2.65 b_i$, the time scale for the secondary flow is

$$T_{flow} \propto \frac{l_A + l_B}{\sqrt{r_{id}\Delta g'}} = 1.65\sqrt{\frac{b_i}{2.65\Delta g'}}. \tag{A 1}$$

Therefore,

$$\frac{T_{dis}}{T_{flow}} \propto \frac{\sqrt{2.65}}{1.65} \approx 0.98, \tag{A 2}$$

i.e. the time scale associated with the interfacial deflections is approximately the same as the time scale for the secondary flow. Therefore, one would anticipate the secondary flow to be quasi-steady.

Appendix B. Potential energy of two-layer fluid in the displaced state and equilibrium state

For $r > r_{id}$, the depths of the upper and lower layers are unaffected by interfacial tilting. Hence, the potential energy outside the zone of interfacial deflection PE_{out} remains unchanged from the equilibrium state. The potential energy of the two-layer fluid in the displaced state is then

$$\mathrm{PE}_{dis} = \int_V \rho g z \,\mathrm{d}V = \frac{1}{2}\pi\rho_2 g r_{id}^2 D^2 \left(1 + 2\frac{h}{D} + \frac{\rho_1}{\rho_2}\frac{h^2}{D^2}\right) + \pi\rho\Delta g' b_i^2 \eta^2 + \mathrm{PE}_{out}, \tag{B 1}$$

where V denotes volume and $D = H - h$ is the upper-layer depth of the equilibrium state. In (B 1) we have implicitly assumed that the fountain, the dome and the plume occupy only a small fraction of the total volume of the box so we may ignore the potential energies contained in these regions. By definition, the non-zero potential energy of the equilibrium state PE_{eq} cannot be reduced by any adiabatic rearrangement of fluid parcels and hence this energy is unavailable for conversion into kinetic energy of fluid motion. Given that

$$\mathrm{PE}_{eq} = \frac{1}{2}\pi\rho_2 g r_{id}^2 D^2 \left(1 + 2\frac{h}{D} + \frac{\rho_1}{\rho_2}\frac{h^2}{D^2}\right) + \mathrm{PE}_{out}, \tag{B 2}$$

and $\mathrm{PE}_{dis} > \mathrm{PE}_{eq}$, subtracting (B 2) from (B 1) gives the available potential energy APE (2.14).

Appendix C. Buoyancy of the impinging fountain

We seek the buoyancy g_i' (2.19) of the fluid supplied by the impinging fountain to the interfacial dome (figure 7). Conservation of buoyancy for the dome requires

$$g_i' Q_i = g_d' Q_d, \quad g_i' = g\left(\frac{\rho_i - \rho_2}{\rho}\right), \quad g_d' = g\left(\frac{\rho_d - \rho_2}{\rho}\right), \tag{C 1}$$

where Q_i and Q_d are the fluxes of volume into and out of the dome, respectively. The outflow from the dome via the annular region is turbulently mixed with the fluid in the lower layer. This is consistent with our argument (§ 2.4) that the fountain's downflow (which is fed by the outflow from the dome) is fully incorporated into the lower layer. Our model assumes that the upper and lower layers are of uniform density. Thus, the density ρ_d of the fluid entering the lower layer equals the density of the lower layer. As $Q_d = Q_i + Q_e$, substituting $\rho_d = \rho_1$ in (C 1) gives

$$\breve{g}_i' = \frac{g_i'}{\Delta g'} = \frac{Q_i + Q_e}{Q_i}. \tag{C 2}$$

Owing to the dependence of $\breve{g}_i'$ on E_i, it is no longer possible to analytically solve (2.20) for E_i. To proceed, we non-dimensionalise equation (2.28) describing the entrainment mechanism for the dome. We recall that the equations describing the conservation of volume and momentum for the dome were combined to form a single expression (2.20). Thus, the non-dimensional equations governing E_i are, from (2.20) and (2.28), respectively,

$$E_i^2 + 2E_i = \frac{2}{3k^4}\frac{\hat{z}_d^5 \breve{g}_i'}{Fr_i^2} - \frac{2}{3k^2}\frac{\hat{z}_d^3 \breve{g}_i'}{Fr_i^2} - \frac{1}{k^2}\hat{z}_d^2, \quad E_i = \frac{\hat{z}_d^2}{k}\left(\frac{C\hat{z}_d^{1/2}}{Fr_i} + \frac{\pi}{2}\tilde{u}_2\right). \tag{C 3}$$

Noting that the quantities $\hat{z}_d$, $\tilde{u}_2$ and $\breve{g}_i'$ are given by (2.29), (2.16) and (C 2), respectively, (C 3) can be solved to obtain E_i for a given $\{Fr_i, \lambda_i\}$. To calculate Fr_i and λ_i, we follow the solution procedure outlined in § 2.4. Figure 15 plots E_i against Fr_i for $\breve{g}_i' = 1$ and when $\breve{g}_i'$ is given by (C 2). Evidently, the two solutions are graphically indistinguishable for $Fr_i \lesssim 0.6$ and the difference between the solutions is less than 4 % at $Fr_i = 0.8$. Hence, our simplifying assumption that $\breve{g}_i' \approx 1$ has only a minor effect on the final solution. This simplification enables us to obtain an analytic solution (2.33) for E_i and deduce the scaling of E_i on Fr_i in the small-λ_i and large-λ_i limits.

Appendix D. Simplified solution for the entrainment flux E_i

For $Fr_i < 1$ and $\lambda_i < 1$, a two-step procedure reduces (2.32) to a simple analytic solution that closely approximates the full solution. First, as $B \approx 0.94$ (2.29), the third term within the parenthesis of (2.31*a*) is sufficiently small compared with $2B/3$ that it may be neglected when $a_3^2 \ll 2B/3 \approx 0.6$. Second, with $C \approx 0.16$ (2.28), upon examining the relative magnitudes of the two terms $((a_2/2)^2, (a_1/3)^3)$ within the square-root in (2.32), we find that

$$\frac{(a_2/2)^2}{(a_1/3)^3} = \frac{27a_2^2}{4a_1^3} \ll 1 \quad \text{for } \lambda_i \ll \frac{64}{\pi^2 B^2 Fr_i^6}\left\{\frac{(1+2B/3)^{3/2}}{\sqrt{18B}} - B^{3/2} C Fr_i^2\right\}^2. \tag{D 1}$$

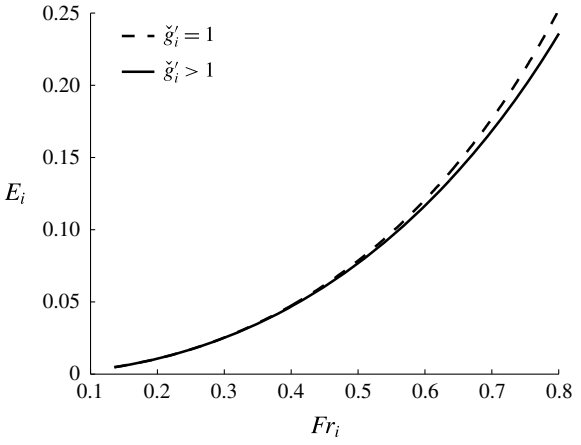

FIGURE 15. Entrainment flux E_i against interfacial Froude number Fr_i for $\breve{g}_i' = 1$ (dashed line) and when $\breve{g}_i'$ is given by (C 2) (solid line). Solutions obtained for $\psi = 25$ and $\mathscr{L} = 0.1$.

Noting that our approximation holds for $\lambda_i \ll 0.9$ when $Fr_i = 1$, and given that λ_i is inversely proportional to Fr_i, this constraint (D 1) on λ_i is satisfied for the range of Fr_i considered. Restricting our attention to these values of λ_i, we may simplify the full solution (2.32) to

$$E_i = \mathbb{R}\left\{\sqrt{\frac{a_1}{3}}\left(\mathrm{i}^{1/3} + (-\mathrm{i})^{1/3}\right)\right\}, \quad \left.\begin{array}{c} \mathrm{i}^{1/3} = \{-\mathrm{i},\ (\sqrt{3}+\mathrm{i})/2,\ (-\sqrt{3}+\mathrm{i})/2\}, \\ (-\mathrm{i})^{1/3} = \{\mathrm{i},\ (-\sqrt{3}-\mathrm{i})/2,\ (\sqrt{3}-\mathrm{i})/2\}, \end{array}\right\} \tag{D 2}$$

where $\mathrm{i} = \sqrt{-1}$. The only solutions for $\mathrm{i}^{1/3}$ and $(-\mathrm{i})^{1/3}$ that yield real, positive values of E_i are $\mathrm{i}^{1/3} = (\sqrt{3}+\mathrm{i})/2$ and $(-\mathrm{i})^{1/3} = (\sqrt{3}-\mathrm{i})/2$. Substituting $\mathrm{i}^{1/3} = (\sqrt{3}+\mathrm{i})/2$ and $(-\mathrm{i})^{1/3} = (\sqrt{3}-\mathrm{i})/2$ in (D 2) gives the analytic solution (2.33).

REFERENCES

BAINES, W. D. 1975 Entrainment by a plume or jet at a density interface. *J. Fluid Mech.* **68** (2), 309–320.

BAINES, W. D., CORRIVEAU, A. F. & REEDMAN, T. J. 1993 Turbulent fountains in a closed chamber. *J. Fluid Mech.* **255**, 621–646.

CARDOSO, S. S. S. & WOODS, A. W. 1993 Mixing by a turbulent plume in a confined stratified region. *J. Fluid Mech.* **250**, 277–305.

CHING, C. Y., FERNANDO, H. J. S. & NOH, Y. 1993 Interaction of a negatively buoyant line plume with a density interface. *Dyn. Atmos. Oceans* **19**, 367–388.

COFFEY, C. J. & HUNT, G. R. 2010 The unidirectional emptying box. *J. Fluid Mech.* **660**, 456–474.

COTEL, A. J., GJESTVANG, J. A., RAMKHELAWAN, N. N. & BREIDENTHAL, R. E. 1997 Impingement of buoyancy-driven flows at a stratified interface. *Exp. Fluids* **23**, 155–160.

DEVENISH, B. J., ROONEY, G. G., WEBSTER, H. N. & THOMSON, D. J. 2010 The entrainment rate for buoyant plumes in a crossflow. *Boundary-Layer Meteorol.* **134**, 411–439.

FERNANDO, H. J. S. 1991 Turbulent mixing in stratified fluids. *Annu. Rev. Fluid Mech.* **23**, 455–493.

HOULT, D. P. & WEIL, J. C. 1972 Turbulent plume in a laminar cross flow. *Atmos. Environ.* **6**, 513–531.

HUNT, G. R. & BURRIDGE, H. C. 2015 Fountains in industry and nature. *Annu. Rev. Fluid Mech.* **47**, 195–220.

HUNT, G. R. & COFFEY, C. J. 2010 Emptying boxes: classifying transient natural ventilation flows. *J. Fluid Mech.* **646**, 137–168.

JIRKA, G. H. & HARLEMAN, D. R. F. 1979 Stability and mixing of a vertical plane buoyant jet in a confined depth. *J. Fluid Mech.* **94**, 275–304.

KAYE, N. B. & HUNT, G. R. 2006 Weak fountains. *J. Fluid Mech.* **558**, 319–328.

KAYE, N. B. & LINDEN, P. F. 2004 Coalescing axisymmetric turbulent plumes. *J. Fluid Mech.* **502**, 41–63.

KUMAGAI, M. 1984 Turbulent buoyant convection from a source in a confined two-layered region. *J. Fluid Mech.* **147**, 105–131.

LEE, J. H. W. & CHU, V. H. 1979 *Turbulent Jets and Plumes: A Lagrangian Approach*. Kluwer Academic.

LIN, Y. J. P. & LINDEN, P. F. 2005 The entrainment due to a turbulent fountain at a density interface. *J. Fluid Mech.* **542**, 25–52.

LINDEN, P. F. 1974 The interaction of a vortex ring with a sharp density interface: a model for turbulent entrainment. *J. Fluid Mech.* **60** (3), 467–480.

MIZUSHINA, T., OGINO, F., TAKEUCHI, H. & IKAWA, H. 1982 An experimental study of vertical turbulent jet with negative buoyancy. *Wärme-Stoffübertrag.* **16**, 15–21.

MORTON, B. R., TAYLOR, G. & TURNER, J. S. 1956 Turbulent gravitational convection from maintained and instantaneous sources. *Proc. R. Soc. Lond.* A **234**, 1–23.

SHRINIVAS, A. B. & HUNT, G. R. 2014 Unconfined turbulent entrainment across density interfaces. *J. Fluid Mech.* **757**, 573–598.

SHY, S. S. 1995 Mixing dynamics of jet interaction with a sharp density interface. *Exp. Therm. Fluid Sci.* **10**, 355–369.

TURNER, J. S. 1986 Turbulent entrainment: the development of the entrainment assumption, and its application to geophysical flows. *J. Fluid Mech.* **173**, 431–471.